Near Surface Geophysics

EAGE EUROPEAN ASSOCIATION OF GEOSCIENTISTS & ENGINEERS

Near Surface Geophysics, 2020, **18**, 23–37 doi: 10.1002/nsg.12068

Automated static and moveout corrections of high-resolution seismic data from the Baltic Sea

Sönke Reiche[1]*, Benjamin Berkels[2,3] and Benedikt Weiß[4]

[1]*Institute for Applied Geophysics and Geothermal Energy, RWTH Aachen University, Mathieustr. 10, 52074 Aachen, Germany,* [2]*AICES Graduate School, RWTH Aachen University, Schinkelstr. 2, 52062 Aachen, Germany,* [3]*Institute for Geometry and Practical Mathematics, RWTH Aachen University, Templergraben 55, 52056 Aachen, and* [4]*Faculty of Geosciences, University of Bremen, Klagenfurter Str., 28359 Bremen, Germany*

Received April 2019, revision accepted August 2019

ABSTRACT

High-frequency multichannel seismic systems provide detailed images of the shallow marine subsurface. In order to exploit the redundancy inherent in such data optimally, traveltime corrections need to account for normal moveout and static effects due to vertical source and receiver variations. Misalignment of reflections in common-midpoint gathers will significantly lower the frequency content in the final stack, making this correction particularly important for very high-frequency seismic data. Traditionally, normal moveout correction involves labour-intensive picking of stacking velocities, while static corrections can be, by some techniques, performed automatically. In this paper, we present a high-frequency seismic case study from the Baltic Sea, using seismic image matching as a novel, fully automated technique to perform joint moveout and static corrections. Our multichannel test profiles were acquired offshore Rügen island for wind farm development. Owing to the regular passage of up to 1.5 m high ocean waves during data acquisition, these boomer profiles suffer from strong static effects. We perform joint normal moveout and static corrections by defining the nearest common offset section as a fixed reference frame and minimizing its difference in traveltime with respect to all available common offset sections. Time shifts are computed independent of a pre-defined traveltime curve, using the normalized cross-correlation as a measure of data similarity while penalizing irregular displacements by a regularization term. Time shifts are converted to stacking velocities based on the traditional hyperbolic traveltime equation. Our results are compared with those derived by conventional manual velocity analysis and subsequent trim static corrections. We find that image matching produces stacks of similar quality and stacking velocity models of similar to slightly better quality compared with the conventionally derived ones, revealing the potential of this technique to automatize and significantly speed up this first part of the seismic processing chain.

Key words: Boomer, Offshore wind farm site survey, Seismic processing, Seismic image matching, Velocity analysis.

INTRODUCTION

Very-high-resolution (VHR) marine seismic data are acquired with source frequencies above 1 kHz and provide a subseafloor resolution on the decimetre scale (Missiaen 2005). Such detailed images are increasingly used to address archaeological (Müller *et al.* 2009; Mueller, Woelz and Kalmring 2013) and geological questions (Novak and Pedersen 2000; Stoker *et al.* 2006) as well as for offshore engineering

*E-mail: s.reiche@gmx.de

purposes (Missiaen and Feller 2008; Leth and Novak 2010). To optimize data acquisition, novel acquisition systems were constructed recently, aiming to provide high-quality and cost-effective subsurface information (Missiaen, Versteeg and Henriet 2002; Scheidhauer, Maerillier and Dupuy 2005; Müller *et al.* 2009; Monrigal, de Jong and Duarte 2017).

Processing of newly collected data can be a labour-intensive procedure, particularly for surveys using offsets sufficiently large for demanding the search for stacking velocities. In addition, many VHR data sets suffer from sea-state–induced static effects, with vertical displacements sometimes exceeding the dominant wavelength of the seismic signal (Marsset *et al.* 1998; Missiaen 2005). Misalignment of traces in common-midpoint (CMP) gathers will cause destructive interference and loss of higher frequencies in the final stack, making accurate normal moveout (NMO) and static corrections particularly important for VHR multichannel marine seismic data (Kluesner *et al.* 2018).

Using high-resolution multichannel watergun data acquired across the Bengal Fan, Gutowski, Breitzke and Spieß (2002) proposed two methods to perform static corrections. Their first approach relies on the availability of simultaneously acquired sub-bottom profiler data. The correction strategy involves automated detection of the seafloor reflection within both data sets, followed by matching of picks from NMO-corrected watergun gathers to picks associated with a spatially coinciding sub-bottom profiler trace. This approach worked well for flat seafloor topography but failed in regions where seafloor inclination exceeded the imaging capabilities of the sub-bottom profiler system. Thus, Gutowksi, Breitzke and Spieß (2002) proposed a second correction strategy, relying on the watergun data only. Here, seafloor reflection picks from NMO-corrected shot gathers are linearly detrended, removing the effect of seafloor morphology from intra-gather time variations. The remaining traveltime differences are quantified as static shifts. As these are determined from a limited number of shot gathers for the entire seismic line, this method is restricted to account for constant streamer bending rather than for variable movement of the acquisition system during the survey.

Wardell, Diviacco and Sinceri (2002) proposed a technique centred on 'common offset spatial averaging'. For a 2D seismic line, seafloor picks are sorted into a 3D surface with shot number and offset on the horizontal axes. Next, first arrival times along each common offset (CO) section are averaged. Averaged values are subtracted from the initial picks, isolating time variations caused by static effects and seafloor morphology. The latter component is subtracted by removing the mean residual traveltime from each CMP gather, resulting in a final surface where differences in traveltime are purely related to wave and swell effects. This approach has successfully proven to remove static effects from VHR marine seismic data (Wardell *et al.* 2002; Duarte, Wardell and Monrigal 2017).

Another static correction approach was recently applied by Jones (2013) and Kluesner *et al.* (2018). Using high-resolution sparker data, traces within each NMO-corrected CMP gather were cross-correlated with a pilot trace (e.g. a stack of all traces contained within the gather). For each trace, time shifts that maximize the cross-correlation were used to perform the static corrections. Whereas this automated approach worked well for correcting intra-gather statics (Jones 2013; Kluesner *et al.* 2018), it does not account for along-profile static effects.

These examples demonstrate how recent developments address and increasingly automatize the correction of static shifts, providing solutions specifically tailored to VHR marine seismic data. In contrast, NMO correction and velocity analysis is still mainly done manually by picking stacking velocities which maximize the coherency of NMO-corrected gathers. Acquisition systems using short receiver cables may automatize this step by using constant stacking velocities (Müller *et al.* 2009). However, accurate velocities are required to produce high-quality stacks in case of longer-offset VHR systems.

Some techniques exist to perform NMO correction and determination of stacking velocities automatically (Adler and Brandwood 1999; Siliqi *et al.* 2003). However, these approaches commonly prescribe some model on the geometry of seismic traveltime curves. Reiche and Berkels (2018) recently introduced 'seismic image matching' as a technique to perform automated NMO correction and stacking velocity analysis without imposing any prior assumptions on the geometry of traveltime curves. Therefore, this technique is particularly suited for data containing non-hyperbolic events, opening up the possibility to perform joint static and NMO corrections on VHR marine seismic data.

In this study, we present a VHR seismic case study from the Baltic Sea. The primary aim of this work is to test the capabilities of seismic image matching relative to a conventional processing approach using two seismic profiles acquired with a boomer source. Below, we first introduce the seismic data set followed by a brief outline of the conventional processing strategy. Subsequently, the principles of seismic image matching are described. In the Results section, we compare stacks and velocity models derived by seismic image matching to those obtained with a careful conventional processing approach. Finally, advantages and limitations of seismic image

matching are discussed, followed by the main conclusions of this work.

DATA AND METHODS

Data acquisition and pre-processing

High-resolution seismic data sets were acquired during October 2016 in the Baltic Sea, approximately 40 km offshore Rügen island (Spieß 2016, Unpublished F.S. Alkor Cruise Report, Cruise AL486, September 30–November 14. Department of Geosciences, University of Bremen, Bremen, pp. 1–139; Fig. 1). We encountered slight to moderate sea state during data acquisition with wave heights of up to 1.5 m for Line 1 and up to 1 m for Line 2. The spread was towed by the research vessel ALKOR, moving at an average velocity of 3 to 3.5 kn. Here, we only use a fraction of the entire data set, consisting of two selected 2D lines (Fig. 1). Seismic energy was released at a shot interval of 0.33 s for Line 1 and 0.25 s for Line 2, using a boomer source with frequencies from 500 to 5000 Hz. With a sampling rate of 8000 Hz, the recorded data sets are slightly undersampled, limiting the maximum frequency to approximately 3500 Hz. Reflected energy was recorded by a 64-channel analogue streamer with a channel spacing of 1 m for the closer 32 channels and 4 m for the more distant 32 channels. For this study, only the first 32 channels are used as exclusion of the far-offset channels, which show a poor signal-to-noise ratio, generally led to an increase in the quality of the resulting stacks. The streamer was towed at a depth of approximately 0.8 m with an initial offset of 21 m between the source and the first channel. Three bird units controlled the streamer position, placed near channels 1, 32 and 64, respectively. Source and receiver coordinates were computed by linearly extrapolating the ship's GPS data along the ship track, accounting for the distance between the GPS antenna and seismic source and receivers. Data were recorded for a total duration of 0.22 s for each shot. Seismic traces were sorted into common-midpoint (CMP) gathers with a CMP spacing of 0.5 m, resulting in a fold of approximately 25 to 35. Pre-processing steps included removal of a DC bias, low-cut filtering (frequencies: 100–200 Hz), removal of the direct wave and trace editing.

Conventional processing: normal moveout and static corrections

We determined stacking velocities by manually picking of semblance-based coherence maxima at every 50th CMP. Semblance maxima were calculated along a range of hyperbolic traveltime curves with the best-fit hyperbola maximizing the energy to be stacked. Based on the final stacking velocity model, each CMP was NMO corrected. NMO-corrected traces contain significant residual moveout due to ocean wave–induced vertical changes in source and receiver positions. Following the approach by Jones (2013) and Kluesner *et al.* (2018), non-surface consistent trim static corrections were applied by cross-correlating traces contained within each CMP gather with a stacked pilot trace along a pre-defined window that is centred on the seafloor reflection. For Line 1, we used a window size from 0.05 to 0.064 s two-way traveltime (TWT) and for Line 2 from 0.056 to 0.061 s TWT. We note that this approach corrects for intra-gather static variations only. Post-stack static variations, expressed as vertical shifts that are best observed along the seafloor reflection, are not eliminated by the trim statics approach. Therefore, these were removed from the post-stack section as static shifts, calculated by the difference between the running average of the seafloor reflection arrival time within a 25-m wide window (50 CMPs) and the time to the seafloor reflection of each individual trace.

Seismic image matching: normal moveout and static corrections

Below, we briefly describe the principles of seismic image matching. For a complete description of this technique, the reader is referred to Reiche and Berkels (2018) and Berkels *et al.* (2014).

Consider a set of 2D seismic CO sections. We now define CO section 1 as the reference image g and all available CO sections as template images, ordered by ascending offset and denoted as $f_1, \ldots, f_n$. Each CO section shall be characterized by exactly the same dimensions with the image domain Ω ranging from $l_{\min}$ to $l_{\max}$ in space direction and from $u_{\min}$ to $u_{\max}$ in time direction. Hence, each CO section must have the same number of traces, being one trace per CMP. For a given template CO section, this is achieved by stacking traces that fall into the same CMP bin while adding zero-valued traces at CMP locations not covered by data. For the reference CO section, which needs to contain data at all CMP locations, missing CMPs are simply filled by duplicating neighbouring traces. This approach differs from the more complicated procedure described in Reiche and Berkels (2018), simply because the VHR data used in this study contained a near-offset trace (i.e. channel 1 trace) at almost all CMP locations.

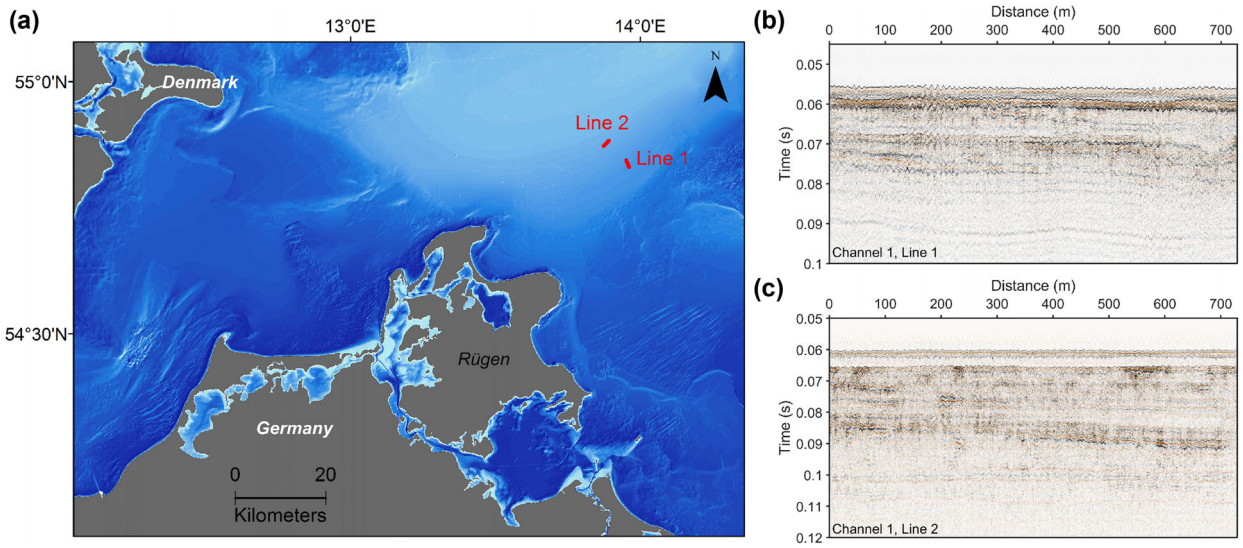

Figure 1 (a) Survey area showing the location of the seismic lines used in this study. (b) Data recorded by channel 1 along Line 1 showing significant static variations along the seafloor reflection. (c) Data recorded by channel 1 along Line 2 similarly suffer from static effects, even though ocean waves were not as high as during acquisition of Line 1.

Seismic image matching now performs the task of transforming each template image $f_1, \ldots, f_n$ into the coordinate system of the reference image g such that $f(l, \varphi(l,u)) \approx g(l,u)$. The scalar-valued deformation φ encodes the shift in time direction that may vary across the image domain, depending on its position (l,u). In particular, the temporal shift at (l,u) is given by $\varphi(l,u) - u$. The deformation is computed by minimizing the objective functional

$$E(\varphi) = D(f \circ (l,\varphi), g) + \lambda R(\varphi), \tag{1}$$

where D quantifies the similarity between the deformed template image $f \circ (l,\varphi)$ (short notation for $f(l,\varphi(l,u))$) and the reference image g by means of the negative normalized cross-correlation. Furthermore, R is a regularizer that measures the smoothness of the deformation with its weight being adjusted by the scalar parameter $\lambda > 0$. More specifically, the regularization term is defined as

$$R(\varphi) = \int_{u_{min}}^{u_{max}} \int_{l_{min}}^{l_{max}} \lambda_l \left|\partial_l \varphi(l,u)\right|^2 + \lambda_u \left|\partial_u \varphi(l,u)\right|^2 + \upsilon(\Delta\varphi(l,u))^2 \mathrm{dldu}, \tag{2}$$

where the integrand represents the weighted sum of the norm of the squared derivative of φ with respect to l, the norm of the squared derivative of φ with respect to u and the squared Laplacian of φ. While an increase in λ_l and λ_u will lead to a smoother deformation field in space and time directions, respectively, increasing υ will lead to an overall, strong smoothing of φ. Since only the three values $\lambda \times \lambda_l$, $\lambda \times \lambda_u$ and $\lambda \times \upsilon$ matter for defining the weights of the regularization term, we can fix any one of the four parameters to a non-zero value and adjust the other values accordingly to receive the same three resulting weights. This step does not affect the results. Therefore, the number of parameters is reduced from four (λ, λ_l, λ_u, υ) to three by setting λ_u to 5.479 s^{-1} (equal to 1 / 0.1825 s, which is the reciprocal of the total record length used in this study).

Note that for a given image matching task, φ may be refined in an iterative manner, each ending with a set of corrected CO sections, which are averaged into a stack, serving as an improved reference image used for a next round of computing φ. Here, we compute φ based on one additional step of refinement.

Seismic image matching was first applied to seismic Line 1 (Fig. 1). In order to correct all input CO sections, $f_1, \ldots, f_{32}$, to g (CO section 1), we used a two-step matching procedure, consisting of two independent image matching tasks: First, after a few test iterations, regularization parameters were chosen as $\lambda = 2$, $\lambda_l = 0.014$ m^{-1} and $\upsilon = 0.002$, leading to a fairly smooth deformation φ. Corrected sections still contained some residual moveout, mainly limited to static effects. We therefore defined these initially corrected CO sections $f_1 \circ (l,\varphi_1), \ldots, f_{32} \circ (l,\varphi_{32})$ as input for a second iteration, where we essentially set λ to 1 and λ_u to ∞ while setting λ_l and υ equal to zero. Note that, numerically, we cannot set λ_u to ∞. Instead, we reparametrized the deformation so

that there is only one degree of freedom for each position l, which forces the deformations to be constant in time direction. Furthermore, the multi-level hierarchy needs to be adjusted to only coarsen the data in temporal direction, not in the spatial direction. For details, we refer to Reiche and Berkels (2018) and to the implementation, which is available at https://github.com/berkels/match-series. This second correction essentially computes a static shift for each trace, without being influenced by neighbouring traces. It is therefore similar to the trim statics step in the conventional processing sequence, except that data similarity is quantified based on the entire seismic trace and not along a pre-defined window centred on the seafloor reflection. As described in Reiche and Berkels (2018), image matching determines time shifts with a sub-sample precision. Using these to map the seismic data to the corresponding discrete sample requires interpolation. As all corrections in this study are based on two individual matching iterations, this mapping has to be performed twice. We use linear interpolation after the first iteration followed by nearest-neighbour interpolation after the second iteration to avoid excessive smoothing that could be induced by multiple linear interpolation steps.

The image matching correction procedure produces one value of φ for each sample and offset. Here, we use φ after the first iteration for conversion to stacking velocities (this approach is justified in the discussion section). Switching to the CMP domain, φ varies with time and offset. Changing to the nomenclature conventionally used in the seismic literature and in Reiche and Berkels (2018), we note that $\varphi = t$, that is, the deformation is equal to the offset-dependent traveltime $t(x, t_0)$, while u, formerly representing the time coordinate in the reference image g, is now termed t_0 and denotes the traveltime at the minimum offset x_{min} (i.e. the offset associated with channel 1). Therefore, $\varphi(x, t_0) = t(x, t_0) = t_0 + \Delta t(x, t_0)$, where $\Delta t(x, t_0)$ is a shift in time direction. Consequently, stacking velocities $v_n(t_0)$ are derived by

$$v_n(t_0) = \sqrt{\frac{x_{min}^2 - x^2}{t_0^2 - t^2(x, t_0)}}. \quad (3)$$

As we have one value of $\varphi(x, t_0)$ for every sample and offset, solving equation (3) similarly yields a stacking velocity model for each offset. In order to reduce these to a single velocity model, we first limit the number of available velocities to those determined at offsets that are neither too small for being sensitive to subsurface velocity variations nor too large for satisfying the hyperbolic traveltime assumption. This is achieved by defining a simple time-offset function that roughly describes an offset-to-target ratio of one, starting at the minimum offset $x = 21$ m at $t = 0$ s TWT and linearly increasing to the maximum offset $x = 52$ m at $t = 0.065$ s TWT (corresponding to 52 m depth, given an average velocity of 1600 m/s). Traveltimes greater than 0.065 s TWT are assigned to the maximum offset. Velocities are now extracted within a $\pm$ 5 m window along this time-offset function. These remaining values are then reduced to a single stacking velocity for each sample by simply computing the median velocity. We note that due to restrictions in streamer length, velocities below 0.065 s TWT are derived from offsets shorter than the target depth, adding a somewhat larger uncertainty towards the base of the velocity model. Finally, all samples above the seafloor reflection are assigned to a water column velocity, approximated to 1500 m/s. This relatively crude approach may be refined by including information from temperature–pressure–conductivity or sounding measurements.

As image matching transforms all input CO sections to t_0 associated with x_{min} instead of the true zero-offset traveltime, some residual moveout remains in the stacked section, depending on the distance between the seismic source and the nearest offset recording channel. Using $\Delta t(x, t_0) \approx \frac{x^2}{2 \cdot v_n^2(t_0) \cdot t_0}$, we estimate this effect at the position of the seafloor reflection with $t_0 = 0.053$ s TWT, $x = 21$ m and $v_n = 1500$ m/s, yielding a residual moveout of 0.00185 s, corresponding to approximately 15 samples. We note that this residual moveout will be much less for deeper reflections. We removed this effect from the stacked sections via post-stack NMO correction using previously derived image-matching velocities. The effect of x_{min} was removed from CMP gathers shown in this paper purely for visual comparison purposes and thus simply by using a constant velocity of 1500 m/s. Finally, the velocity model itself suffers from the same residual moveout – in our case creating a maximum velocity error of approximately 10 m/s, based on an average velocity gradient of 5000 m/s². We consider this velocity error negligible for performing post-stack NMO correction on our final stacked section, as it will affect vertical positioning of the seismic data by an error smaller than the size of one sample.

Finally, all stacks were subject to post-stack static corrections, following the same procedure as described at the end of the 'Conventional processing: normal moveout and static corrections' section

RESULTS

Figure 2 shows a comparison between the conventional and the image matching results for seismic Line 1. Both stacks are generally of similar quality (Fig. 2a,b), which is also reflected

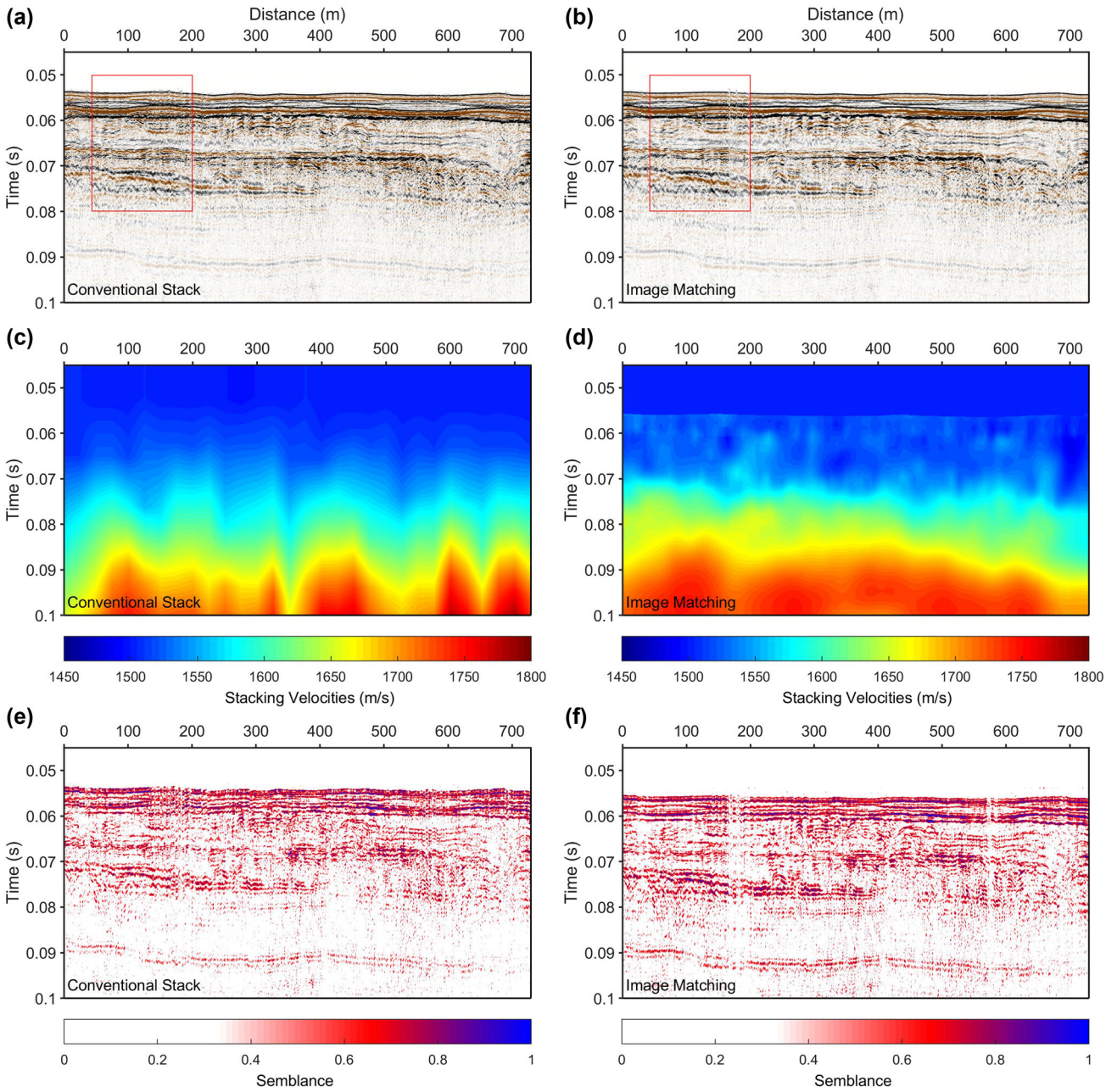

Figure 2 Comparison of conventionally derived and image matching results for seismic Line 1. (a,b) stacked sections, (c,d) stacking velocities and (e,f) semblance sections.

in the coherency distribution displayed in Fig. 2(e,f). However, some differences appear when looking at enlarged sections (Fig. 3a,b). In general, the image matching stack shows a minor loss in resolution compared with the conventional stack (see cyan arrows in Fig. 3b). In addition, we observe local differences in the quality of the static correction results. Between approximately 150 m and 250 m, Line 1 is strongly affected by static effects (see also channel 1 profile in Fig. 1b). In this part of the profile, the image matching stack shows two narrow regions of poorly corrected traces (at approximately $x = 165$ m and $x = 180$ m), which appear slightly shifted upwards when looking at the seafloor reflection. In fact, these artefacts result from failure to correct for the residual moveout after the first image matching iteration (Fig. 3f). In the conventional

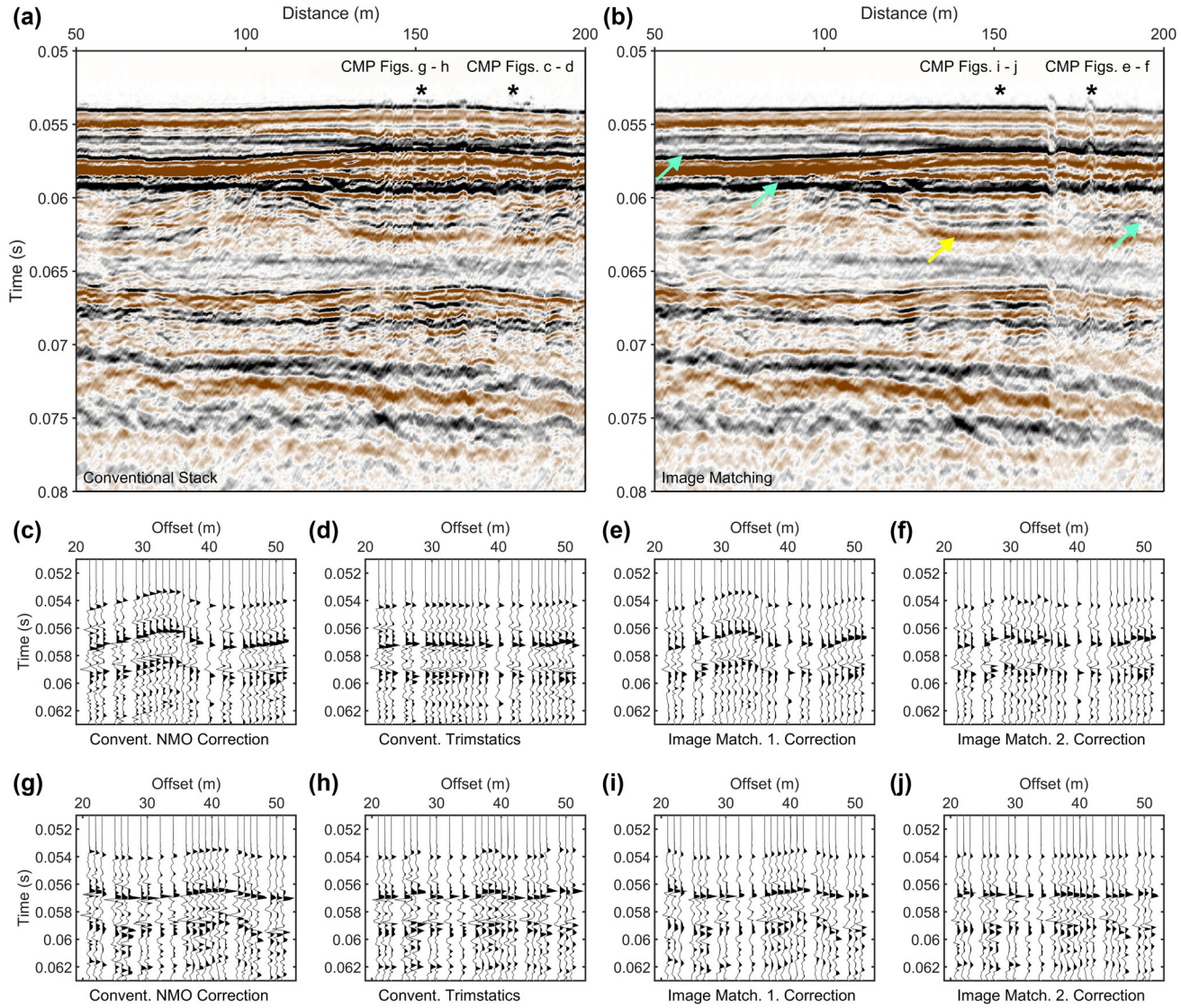

Figure 3 Enlarged sections from seismic Line 1 comparing the quality of (a) the conventional and (b) image matching stacks. The profile location is indicated by red boxes in Fig. 2(a,b). Cyan arrows point to regions where the image-matching stack suffers from a slightly lower resolution compared with the conventional stack while the yellow arrow indicates a region where the image-matching stack shows improved reflection continuity. (c) CMP gather after conventional NMO correction and (d) trim statics. (e) The same CMP gather after the first and (f) second image matching iterations. Note the similarity between the correction results shown in (c) and (e). (g) Second example of a CMP gather after NMO correction and (h) trim statics. (i) The same gather after the first and (j) second image matching iterations.

stack, these artefacts are less pronounced (Fig. 3d). Instead, this stack suffers from a broader region ($x = 140$ m to $x = 200$ m in Fig. 3a) of unsatisfactorily corrected traces, as one can also judge by looking at one of the common-midpoint (CMP) gathers from this part of the profile (compare Fig. 3h,j).

Comparison of image matching and conventionally derived stacking velocities shows a large degree of similarity (Fig. 2c,d). However, in more detail, we observe that image-matching velocities display stronger lateral variability within the time interval from approximately 0.055 to 0.075 s two-way traveltime (TWT) compared with conventionally derived ones. Furthermore, below 0.075 s TWT, image-matching velocities become rather smooth and little small-scale variability is observed. In general, image-matching velocities are determined on a sample-by-sample basis, whereas conventional velocities were only picked at every 50th CMP. The lateral variability of conventional velocities thus reflects the distance

of velocity picks, whereas image-matching velocities may, in principle, differ for each sample. Significant small-scale velocity variations will particularly occur in the presence of lateral subsurface heterogeneity that is captured by sufficiently coherent seismic events. Then, the data term D in equation (1) will outweigh the regularization term R, resulting in heterogeneous velocity fields. In the absence of significant seismic reflectivity, as observed below 0.075 s TWT in Fig. 2(a), the regularization term will increasingly dominate, resulting in a smooth velocity field. Both velocity models capture a significant increase in stacking velocities, between 0.07 and 0.095 s TWT. However, looking at the image matching velocity model, this gradient is inclined towards the right-hand side of the profile and closely follows the dip of reflections evident within the stacked section above (Fig. 2b,d).

In order to test the sensitivity of the first image-matching iteration result on the choice of regularization parameters, we systematically varied the three regularization parameters ($\lambda,\ \lambda_l, \upsilon$). This test was performed on the same CMP gather shown in Fig. 3(c–f). Figure 4 displays the corrected CMP gathers along with the chosen set of parameters, and Fig. 5 shows the associated distribution of computed time shifts, that is, $\varphi(x, t_0) - t_0 = \Delta t(x, t_0)$. In a first test, we changed the ratio between the regularization in space and time directions by varying λ_l by two orders of magnitude in each direction (Figs 4a–c and 5a–c). Second, λ, the overall weight of the regularization term, was varied by one order of magnitude in each direction (Figs 4d–f and 5d–f). Finally, we varied υ, affecting the second derivatives of φ, by one order of magnitude in each direction (Figs 4g–i and 5g–i). Neither the corrected gathers nor the corresponding time-shift sections reveal significant differences for any of these parameter variations, making our initial correction result quite robust against parameter variations within the regularization term.

Ideally, a set of chosen regularization parameters for a given seismic line should also yield satisfactory results when applied to other profiles from the same survey. For this purpose, the same correction approach used for Line 1 was also applied to a neighbouring profile, Line 2, located a few kilometres to the northwest (Fig. 1). Results are shown in Fig. 6, and an enlarged section is shown in Fig. 7. Comparing the quality of the conventionally derived stack and the image-matching result reveals that image matching produces a stack of better reflection continuity and slightly reduced noise level (Fig. 6a,b). This is also evident in the enlarged section, where individual reflections appear locally more clearly within the image matching stack (Fig. 7a,b). Unlike seismic Line 1, we cannot observe any loss in resolution in the image-matching stack compared with its conventional counterpart. On the contrary, the image-matching stack displays a couple of small-scale features that are not as clearly observable in the conventional stack (see yellow arrows in Fig. 7b). Comparing semblance plots for both correction results shows generally higher coherencies for the image matching result (Fig. 6e,f).

Judging the flatness of events in CMP gathers reveals similar correction results after normal moveout (NMO) correction and the first image matching iteration (Fig. 7c,e) as well as after applying trim statics and the second image-matching iteration (Fig. 7d,f). However, traces in gathers corrected by seismic image matching show slightly lower amplitudes as well as less noise compared with conventionally corrected ones, particularly for near-offset traces between 0.065 s TWT and 0.075 s TWT. Whereas image matching does not change amplitudes when shifting a given value from t to t_0 (in the sense of t_0 at x_{min}), it relocates these at sub-sample precision. Thus, several amplitude values may then be shifted to almost identical traveltimes, while at other places no data are shifted into the traveltime range corresponding to a given sample. Consequently, the deformed template image requires interpolation to obtain data at discrete samples, which may change absolute values of amplitudes. In addition, should a given amplitude value of a template image not match to any value within the reference image (being an initial stack), its original amplitude may change after deforming and interpolating the template image as it was likely shifted to some sub-sample position that had limited influence on the resulting amplitude after bilinear interpolation. These effects likely reduced amplitudes within the near-offset traces between 0.065 and 0.075 s TWT in Fig. 7(e,f).

Stacking velocity models produced by the conventional and the image matching approach are fairly similar (Fig. 6c,d). As also observed for Line 1, the image matching velocity model displays more lateral heterogeneity in the upper part of the section (0.06–0.1 s TWT) compared with conventional velocities. Both models capture a significant velocity gradient beneath approximately 0.1 s TWT, with the image-matching model showing higher velocities at the base of the model. As there is not much coherent energy in this part of the profile, velocities below 0.11 s TWT are rather a result of manual interpretation (conventional semblance) or regularization (image matching) than being related to data. Within the first half of the profile, at approximately 200 m distance, a region of locally elevated velocities appears in both models. This peak is more pronounced in the conventional velocity model, probably because the weight of the spatial regularization term tends to produce smooth image-matching velocities.

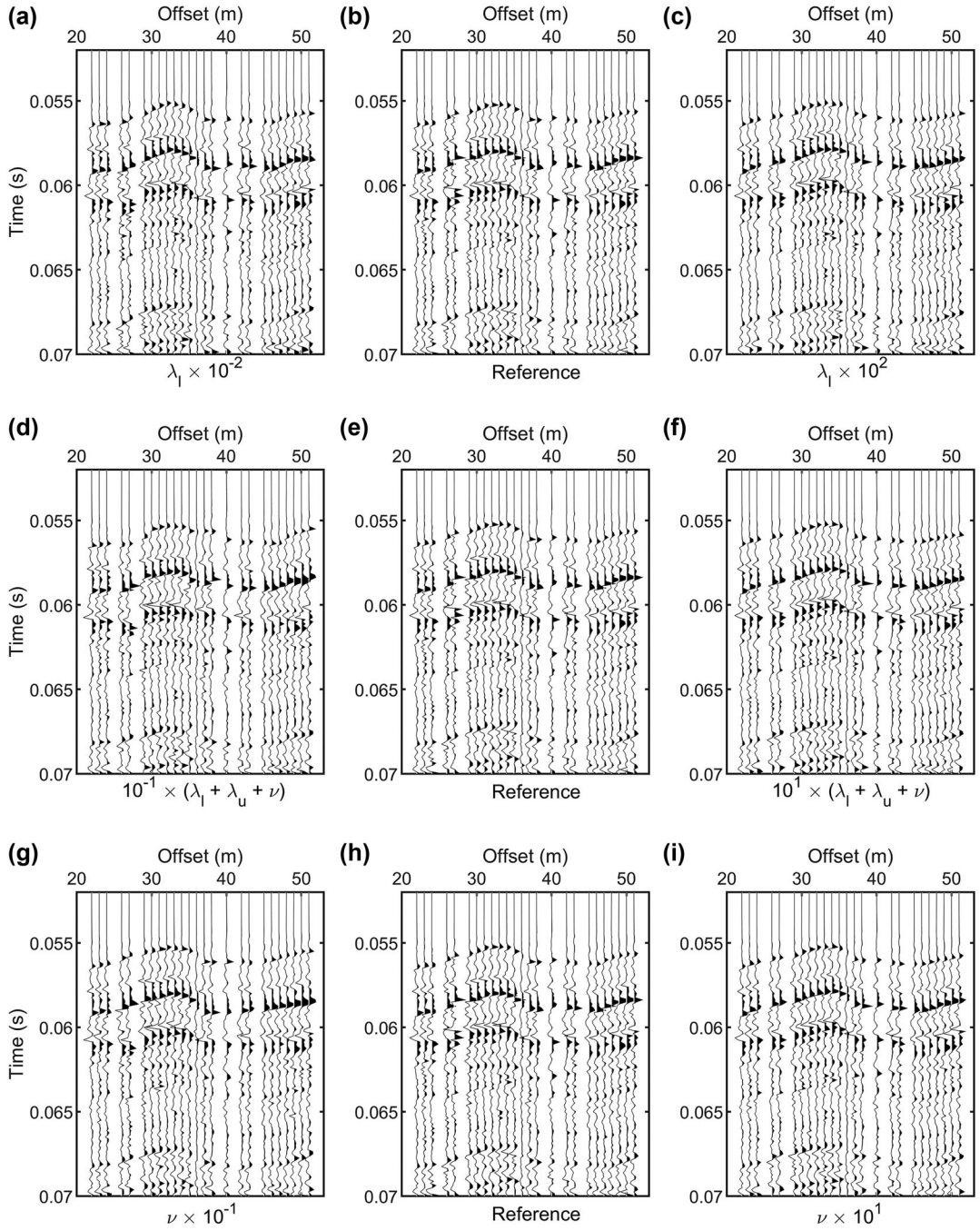

Figure 4 Testing how the choice of regularization parameters influences the first image matching iteration result, using the same CMP gather that is shown in Fig. 3c–f. (a,c) Varying the regularization in space direction by two orders of magnitude relative to the reference choice of parameters ($\lambda = 2$, $\lambda_l = 0.014$ m^{-1} and $\upsilon = 0.002$). (d–f) Varying the overall weight of the regularization term λ by one order of magnitude (the same as changing each parameter by one order of magnitude). (g–i) Varying the weight of υ, associated with the second derivatives, by one order of magnitude. Overall, variations of the regularization parameters in the chosen range do not significantly affect the correction result.

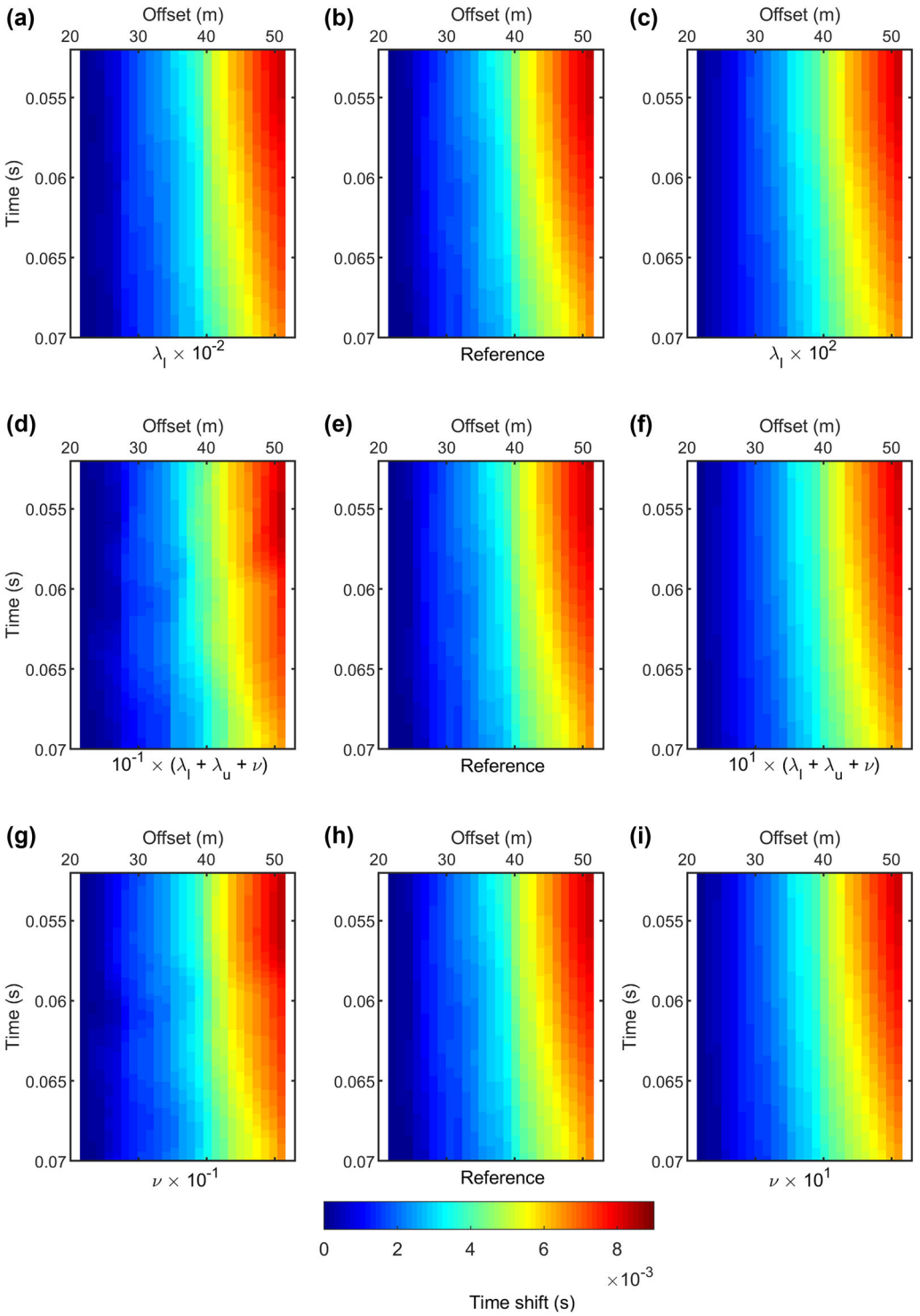

Figure 5 Time shift $\Delta t(x, t_0)$ plots (where $\Delta t(x, t_0) = \varphi(x, t_0) - t_0$) associated with the correction results displayed in Fig. 4. Again, the chosen range of variation of the regularization parameters does not significantly influence the resulting time shift fields.

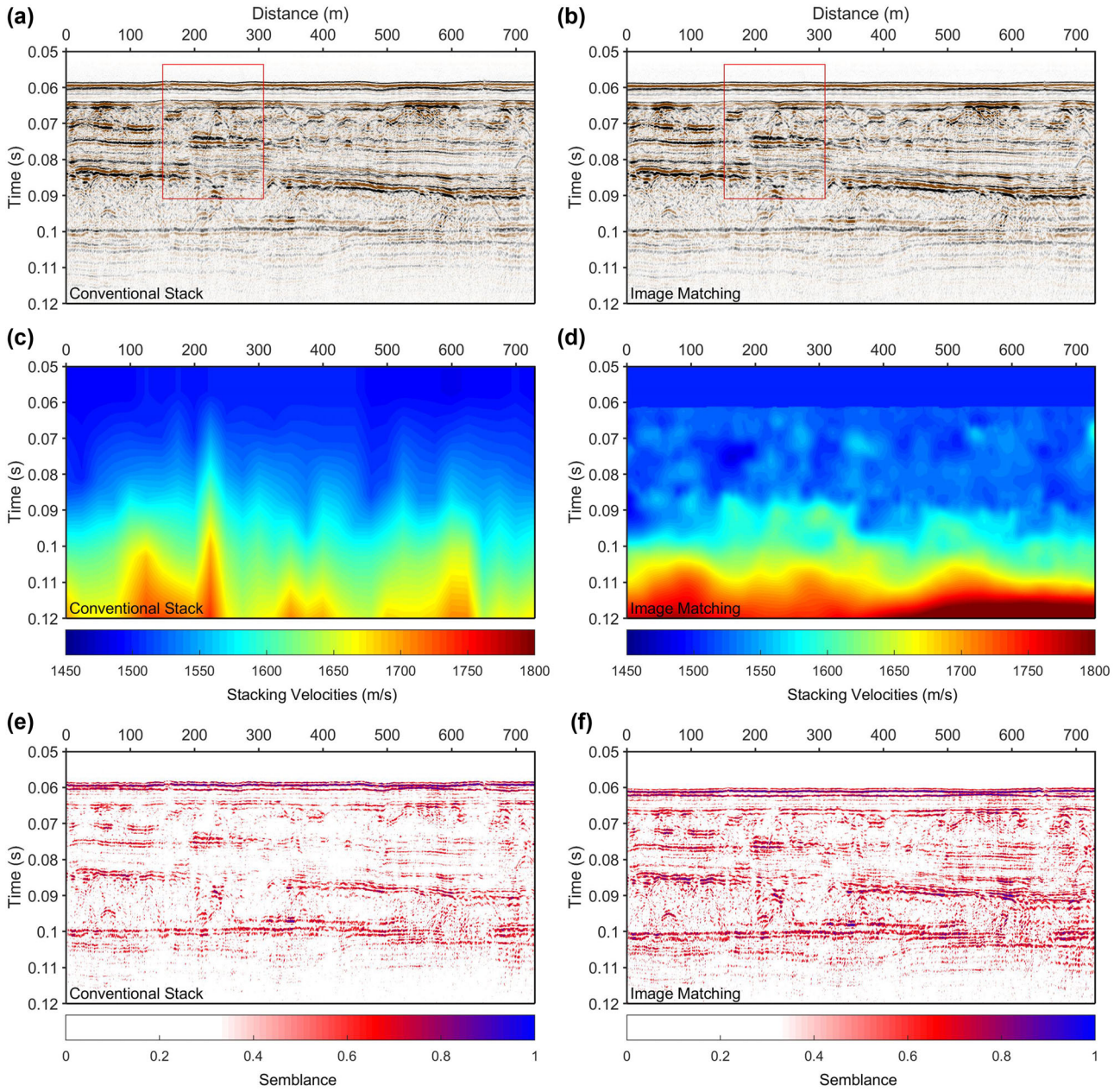

Figure 6 Comparison of conventionally derived and image matching results for seismic Line 2. (a,b) Stacked sections, (c,d) stacking velocities and (e,f) semblance sections.

For Line 2, we observe that the choice of the interpolation approach (linear versus nearest neighbour) used for transforming sub-sample time shifts to discrete samples had a significant effect on the appearance of the resulting image matching stack. While linear interpolation may lead to a loss in resolution and a slight broadening of seismic amplitudes, the nearest neighbour approach will not exploit the potential of sub-sample time shift precision. Figure 8 shows the effect of these two approaches on the quality of the resulting stack along with the corresponding coherency sections. Using nearest-neighbour search after both iterations results in low reflection continuity and moderate coherencies (Fig. 8a,d). Choosing linear interpolation after the first image matching iteration significantly improved the resulting stack and coherency section, no matter what interpolation was used after the second iteration (Fig. 8b,e and 8c,f).

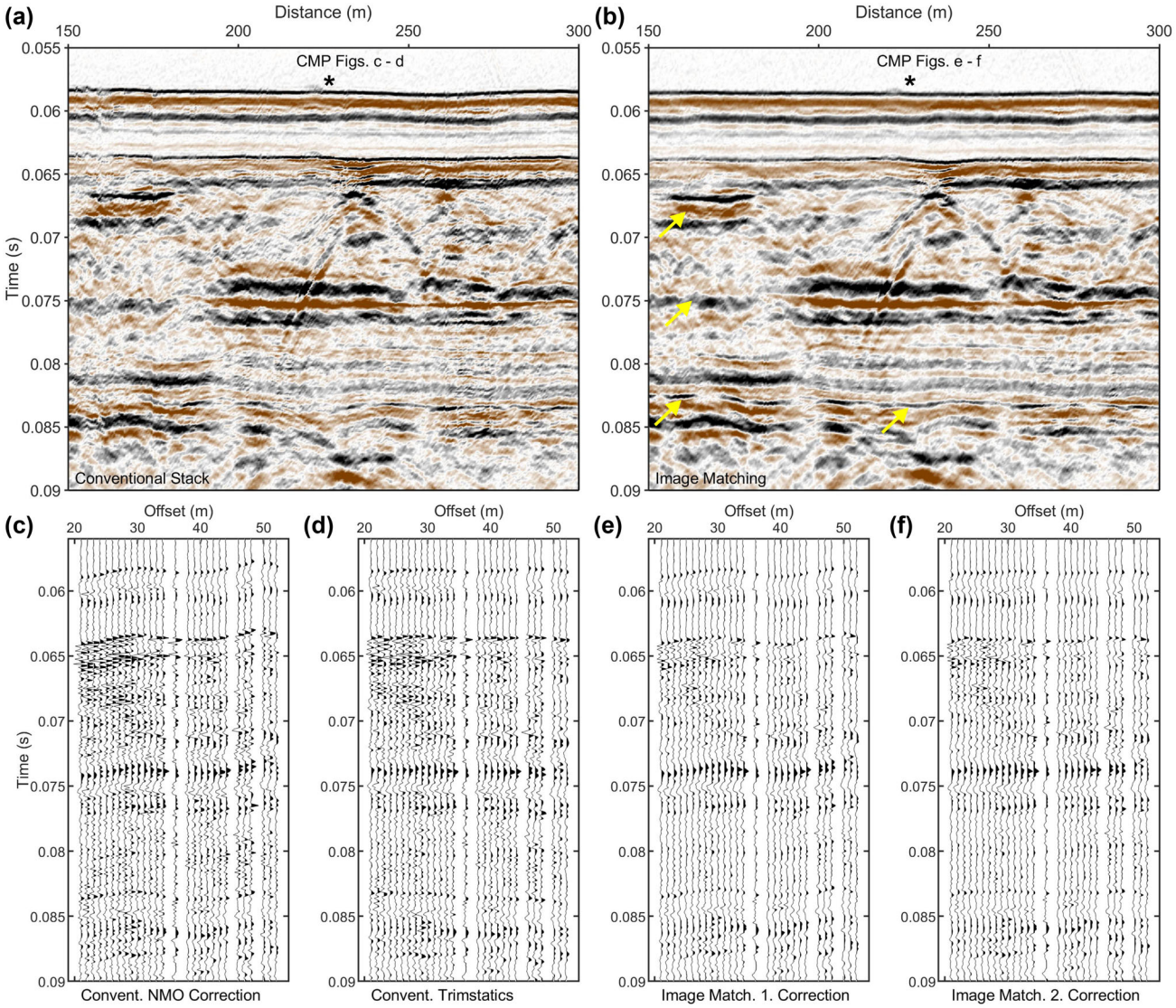

Figure 7 Enlarged sections from seismic Line 2 comparing the quality of (a) the conventional and (b) image matching stacks. The profile location is indicated by red boxes in Fig. 6(a) and (b). Yellow arrows point to regions where the image matching stack shows a better resolution compared with the conventional stack. (c) CMP gather from the centre of the profile after conventional NMO correction and (d) trim statics. (e) The same CMP gather after the first and (f) second image-matching iterations.

DISCUSSION

Seismic image matching represents a novel, fully automated technique, capable of performing joint normal moveout (NMO) and static corrections on very-high-resolution (VHR) marine seismic data. Based on two test profiles, our results demonstrate that image-matching stacks and stacking velocity models may exceed the quality of a careful conventional processing approach. Particularly large VHR data sets would benefit from the automation of this usually very time-consuming part of the seismic processing chain.

When it comes to velocities, we note that in our VHR seismic data set, traveltime variations are caused by both NMO and static effects. Only the former component is physically related to root-mean-square velocities (which basically match stacking velocities, given the level subsurface structure in this region). In the conventional approach, stacking velocities were determined along hyperbolic traveltime curves. Even though static effects broaden coherency peaks during semblance-based velocity analysis (Duarte *et al.* 2017), resulting velocities may still be physically meaningful. For image

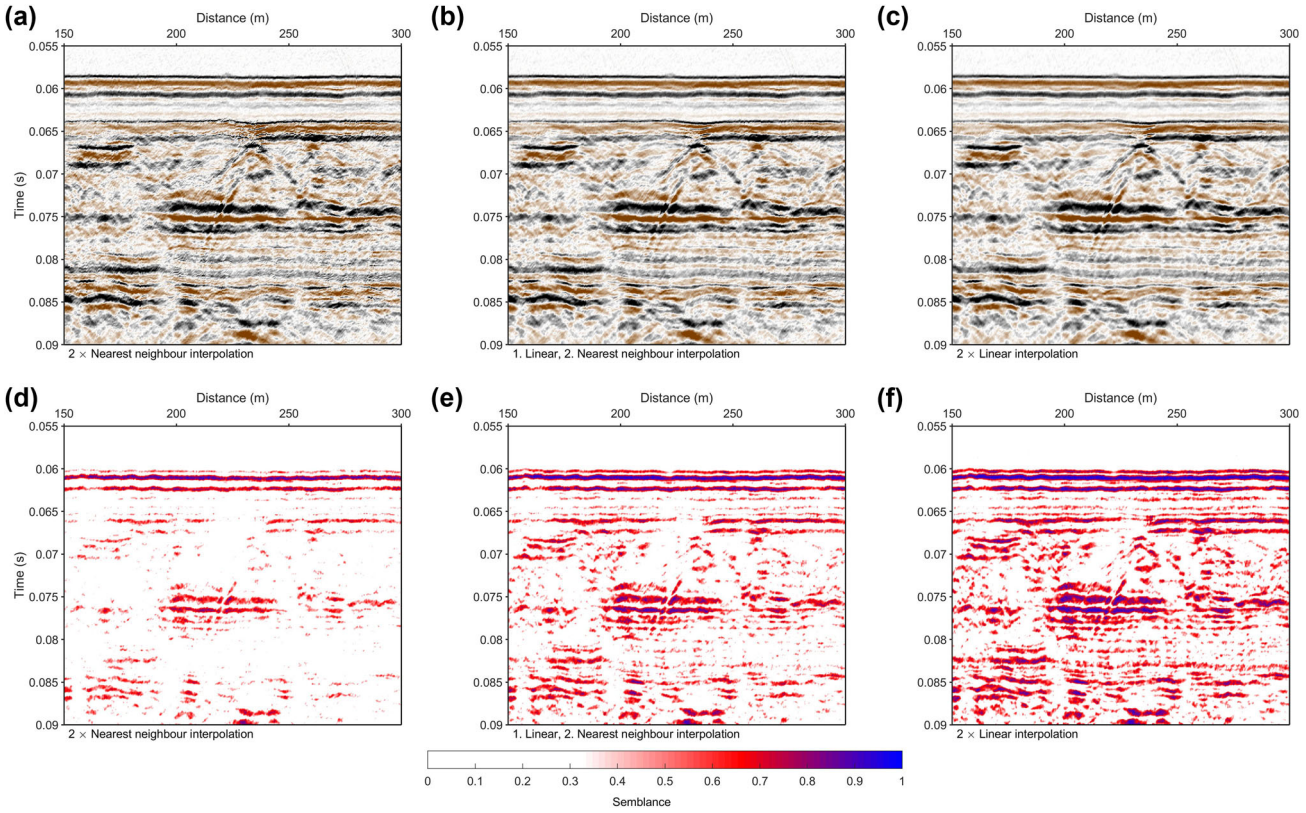

Figure 8 The effect of interpolation on the resulting image matching stack and coherency section, (a,d) using nearest-neighbour interpolation after both image matching iterations, (b,e) using linear interpolation after the first and nearest-neighbour interpolation after the second image-matching iteration and (c,f) using linear interpolation after both image matching iterations.

matching, traveltime corrections do not follow pre-defined traveltime curves, posing a risk of biased stacking velocities if NMO and static effects are corrected together. However, the regularization term in seismic image matching ensures that correction of a given sample will always be influenced by neighbouring samples, avoiding large jumps in the resulting deformation $\varphi(x, t_0)$. Using a two-step correction strategy, the first iteration yields a correction result that strongly resembles the conventional NMO correction result. This is reflected both by broadly consistent velocity models (Figs 2c,d and 6c,d) and in the shapes of corrected traveltime curves, which show very similar residual moveout (compare Fig. 3c and e, Fig. 3g and i as well as Fig. 7c and e). This correction result appears to hold true for a range of regularization parameters (Figs 4 and 5), suggesting that image matching delivers meaningful stacking velocities even for data sets suffering from static effects.

By determining time shifts, and thus stacking velocities, for each sample individually, image-matching velocity models reveal more lateral heterogeneity compared with conventional models, where velocity picks are based on a limited number of traces. Particularly for Line 1, changes in stacking velocities determined by seismic image matching consistently follow seismic reflections (Fig. 2b,d), providing further support for the applicability of this approach. Reliable stacking velocity models are useful for different tasks within the VHR marine seismic processing and interpretation chain: First, given a horizontal subsurface composition, stacking velocities directly serve as input for pre-stack Kirchhoff time migration routines, resulting in interpretable subsurface images. Such time-migrated sections form the basis to infer subsurface petrophysical properties via post-stack impedance inversion, as recently demonstrated by Vardy (2015). Second, offshore engineering tasks, such as wind farm foundations, increasingly benefit from 3D subsurface soil models, even if constructed by lateral interpolation of information derived from 2D seismic lines (Reynolds 2011). As these models are typically required in depth, a simple way, bypassing seismic depth imaging, could be depth conversion via the Dix equation (Dix 1955) using stacking velocities derived from seismic image matching.

Seismic image matching represents a fully automated tool for performing post-NMO static corrections. As time shifts are computed based on data similarity along the entire trace, no search window needs to be specified. In comparison with marine static correction techniques by Gutowski *et al.* (2002), seismic image matching is neither restricted to regions of moderate seafloor inclination nor does it assume static effects to result from a constant bending of the streamer. Instead, the principle of our static correction procedure is similar to trim statics, previously used for VHR data by Jones (2013) and Kluesner *et al.* (2018). While trim statics are computed within the common-midpoint (CMP) domain, aligning each trace to a stacked reference trace, seismic image matching performs static corrections in the CO domain, aligning all input CO section to a stacked section that was computed during a first, more strongly regularized correction iteration. However, during this first iteration, seismic image matching aligns all input CO sections to the first CO section, associated with the nearest offset channel. As this reference image suffers from static effects (Fig. 1b,c), these will, to some extent, also appear in the final stacked sections. Conventional trim statics will suffer from a similar effect, even though such post-stack static variations may be less pronounced. In both cases, post-stack smoothing along the seafloor reflections will visually mitigate this effect but likewise remove existing small-scale seafloor undulations. To overcome this problem, one either needs to include a second set of hydrographic data into the correction approach (Gutowski *et al.* 2002), or account for the traveltime component associated with seafloor morphology in each CMP gather as suggested by Wardell *et al.* (2002).

Despite its ability to perform automated stacking velocity analysis, moveout and static corrections, seismic image matching, at its current stage of development, comes with some limitations. First, in its present implementation our image matching code aims for accuracy rather than speed, being restricted to run on a single CPU only. Thus, correcting a data set of comparable size to those presented in this study requires about half a day on a desktop computer. Parallelization and more efficient implementation would reduce the required time dramatically, but was not our focus in the present study. Second, the penetration depth of seismic data used in this study was restricted mainly to depths above the first seafloor multiple. Seismic image matching cannot differentiate between primary and multiple reflections. Imposing prior restrictions on the search of $\varphi(x, t_0)$, such as an increase in stacking velocities with depth, may somewhat mitigate this problem. Finally, seismic image matching has only been tested on 2D seismic lines. In principle, this technique can be extended to 3D (see discussion in Reiche and Berkels 2018), but further work is required to realize this task.

CONCLUSIONS

In this study, we test the potential of seismic image matching to perform automated stacking velocity analysis, normal moveout and static corrections on very-high-resolution (VHR) marine seismic data. For this purpose, this technique is applied to VHR seismic data from the Baltic Sea. Results are compared with a conventional processing approach, involving manual semblance-based velocity analysis and trim static corrections. We find that image matching is capable of producing stacks of similar and stacking velocity models of similar to slightly better quality compared with conventional results. Regularization parameters, empirically determined on a single seismic line, produced convincing results for a second seismic profile, revealing the potential of this technique to correct data from a whole survey without the need for manual user interaction.

ACKNOWLEDGEMENTS

We thank Volkhard Spieß from the Faculty of Geosciences, University of Bremen for kindly providing the seismic profiles from the Baltic Sea. We further thank Captain Jan Peter Lass and the crew of RV ALKOR for their support during the cruise AL486. B. Berkels was funded in part by the Excellence Initiative of the German Federal and State Governments through grant GSC 111.

REFERENCES

Adler F. and Brandwood S. 1999. Robust estimation of dense 3D stacking velocities from automated picking. SEG 69th Annual International Meeting, October 31–November 5 1999, Houston, USA, Extended Abstracts.

Berkels B., Binev P., Blom D.A., Dahmen W., Sharpley R.C. and Vogt T. 2014. Optimized imaging using non-rigid registration. *Ultramicroscopy* **13**, 46–56.

Dix C.H. 1955. Seismic velocities from surface measurements. *Geophysics* **20**, 68–86.

Duarte H., Wardell N. and Monrigal O. 2017. Advanced processing of UHR3D shallow marine seismic surveys. *Near Surface Geophysics* **15**, 347–358.

Gutowski M., Breitzke M. and Spieß V. 2002. Fast static correction methods for high-frequency multichannel marine seismic reflection data: a high-resolution seismic study of channel-levee systems on the Bengal Fan. *Marine Geophysical Researches* **23**, 57–75.

Jones L.E.A. 2013. High frequency enhancement of sparker sub bottom profiles with multichannel reflection processing. 23rd

International Geophysical Conference and Exhibition, 11–14 August 2013, Melbourne, Australia, Extended Abstracts.

Kluesner J., Brothers D., Hart P., Miller N. and Hatcher G. 2018. Practical approaches to maximizing the resolution of sparker seismic reflection data. *Marine Geophysical Research* **40**, 279–301.

Leth J.O. and Novak B. 2010. Late quaternary geology of a potential wind-farm area in the Kattegat, southern Scandinavia. *Geological Survey of Denmark and Greenland Bulletin* **20**, 31–34.

Marsset B., Missiaen T., De Roeck Y.-H., Noble M., Versteeg W. and Henriet J.P. 1998. Very high resolution 3D marine seismic data processing for geotechnical applications. *Geophysical Prospecting* **46**, 105–120.

Missiaen T. 2005. VHR marine 3D seismics for shallow water investigations: some practical guidelines. *Marine Geophysical Researches* **26**, 145–155.

Missiaen T. and Feller P. 2008. Very-high-resolution seismic and magnetic investigations of a chemical munition dumpsite in the Baltic Sea. *Journal of Applied Geophysics* **65**, 142–154.

Missiaen T., Versteeg W. and Henriet J.-P. 2002. A new 3D seismic acquisition system for very high and ultra high resolution shallow water studies. *First Break* **20**, 227–232.

Monrigal O., de Jong I. and Duarte H. 2017. An ultra-high-resolution 3D marine seismic system for detailed site investigation. *Near Surface Geophysics* **15**, 335–345.

Mueller C., Woelz S. and Kalmring S. 2013. High-resolution 3D marine seismic investigation of Hedeby Harbour, Germany. *The International Journal of Nautical Archaeology* **42**, 326–336.

Müller C., Woelz S., Ersoy Y., Boyce J., Jokisch T., Wendt G. *et al.* 2009. Ultra-high-resolution marine 2D–3D seismic investigation of the Liman Tepe/Karantina Island archaeological site (Urla/Turkey). *Journal of Applied Geophysics* **68**, 124–134.

Novak B. and Pedersen G.P. 2000. Sedimentology, seismic facies and stratigraphy of a Holocene spit–platform complex interpreted from high-resolution shallow seismics, Lysegrund, southern Kattegat, Denmark. *Marine Geology* **162**, 317–335.

Reiche S. and Berkels B. 2018. Automated stacking of seismic reflection data based on non-rigid image matching. *Geophysics* **83**, V171-V183.

Reynolds J.M. 2011. Developments and future trends in near surface geophysics. *First Break* **29**, 69–75.

Scheidhauer M., Maerillier F. and Dupuy D. 2005. Development of a system for 3D high-resolution seismic reflection profiling on lakes. *Marine Geophysical Researches* **26**, 183–195.

Siliqi R., Le Meur D., Gamar F., Smith L., Touré J.P. and Herrmann P. 2003. High-density moveout parameter fields V and η. Part one: Simultaneous automatic picking. 73rd SEG International Exposition and annual Meeting, 26–31 October 2003, Dallas, USA, Extended Abstracts.

Stoker M., Bradwell T., Wilson C., Harper C., Smith D. and Brett C. 2006. Pristine fjord landsystem revealed on the sea bed in the Summer Isles region, NW Scotland. *Scottish Journal of Geology* **42**, 89–99.

Vardy M. 2015. Deriving shallow-water sediment properties using post-stack acoustic impedance inversion. *Near Surface Geophysics* **13**, 143–154.

Wardell N., Diviacco P. and Sinceri R. 2002. 3D pre-processing techniques for marine VHR seismic data. *First Break* **20**, 457–466.

